Nanoscale

COMMUNICATION

View Article Online
View Journal | View Issue

Cite this: *Nanoscale*, 2017, **9**, 12316

Received 22nd June 2017,
Accepted 2nd August 2017

DOI: 10.1039/c7nr04501h

rsc.li/nanoscale

Superior stability for perovskite solar cells with 20% efficiency using vacuum co-evaporation†

Xuejie Zhu,[a] Dong Yang,*[a,d] Ruixia Yang,[b] Bin Yang,[b] Zhou Yang,[a] Xiaodong Ren,[a] Jian Zhang,[c] Jinzhi Niu,[a] Jiangshan Feng[a] and Shengzhong (Frank) Liu *[a,b]

Chemical composition and film quality are two key figures of merit for large-area high-efficiency perovskite solar cells. To date, all studies on mixed perovskites have used solution-processing, which results in imperfect surface coverage and pin-holes generated during solvent evaporation, execrably influencing the stability and efficiency of perovskite solar cells. Herein, we report our development using a vacuum co-evaporation deposition method to fabricate pin-hole-free cesium (Cs)-substituted perovskite films with complete surface coverage. Apart from the simplified procedure, the present method also promises tunable band gap, reduced trap-state density and longer carrier lifetime, leading to solar cell efficiency as high as 20.13%, which is among the highest reported for planar perovskite solar cells. The splendid performance is attributed to superior merits of the Cs-substituted perovskite film including tunable band gap, reduced trap-state density and longer carrier lifetime. Moreover, the Cs-substituted perovskite device without encapsulation exhibits significantly higher stability in ambient air compared with the single-component counterpart. When the Cs-substituted perovskite solar cells are stored in dark for one year, the PCE remains at 19.25%, degrading only 4.37% of the initial efficiency. The excellent stability originates from reduced lattice constant and relaxed strain in perovskite lattice by incorporating Cs cations into the crystal lattice, as demonstrated by the positive peak shifts and reduced peak width in X-ray diffraction analysis.

Introduction

Hybrid organic–inorganic halide perovskite has been considered as an attractive candidate for low-cost solar cell applications due to its high power conversion efficiency (PCE) and straightforward fabrication process.[1–5] In just a few years, the PCE of the perovskite solar cells (PSCs) has been raised from 3.8% to >22%[6–10] by improved interface engineering,[11,12] device optimization[13,14] and perovskite composition.[15,16] The high performance is mainly attributed to the outstanding properties of perovskite materials, such as large absorption coefficient, long carrier diffusion length, favorable direct band gap and high tolerance to defects.[17–19]

At present, all high-efficiency PSCs use organic–inorganic hybrid lead trihalide perovskites with chemical formula ABX_3 as photoactive materials, where typically A is methylammonium (MA) or formamidinium (FA) cations, B is lead, and X is a halide.[20,21] To further improve the solar cell performance, a variety of mixed perovskite materials are developed. For example, mixed halide was used to tune the band gap and improve carrier transport to raise open-circuit voltage (V_{oc}).[22,23] A few metal cations including Sn, Ge, and Bi are used to replace lead to generate more environmentally benign materials.[24–26] FA has been used to partially substitute the well-known MA to extend optical absorption further into the near-infrared range to increase short-circuit current density (J_{sc}).[17,27] Cs-doping is used not only to suppress perovskite decomposition (exhibiting better stability to moisture), but also to reduce trap density, leading to improved PSC efficiency.[28,29]

To date, all research on mixed or doped perovskite films use solution-processing. When the solvent evaporates during spin-coating and annealing treatment, it often leaves pin-holes behind, giving imperfect surface coverage. Even though there have been extensive studies using exotic compounds, such as $Pb(SCN)_2$ and PbS, to improve the film coverage and reduce the pin-hole density,[30,31] it generates by-products, resulting in inferior device performance.[32,33] In addition, the solution-processed Cs-doping often generates mixed CsX precipitation

[a]*Key Laboratory of Applied Surface and Colloid Chemistry, National Ministry of Education; Shaanxi Key Laboratory for Advanced Energy Devices; Shaanxi Engineering Lab for Advanced Energy Technology, School of Materials Science and Engineering, Shaanxi Normal University, Xi'an 710119, China. E-mail: dongyang@snnu.edu.cn, szliu@dicp.ac.cn*
[b]*State Key Laboratory of Molecule Reaction Dynamics, Dalian National Laboratory for Clean Energy; iChEM, Dalian Institute of Chemical Physics, Chinese Academy of Sciences, Dalian, 116023, China*
[c]*School of Material Science and Engineering, Guangxi Key Laboratory of Information Materials, Guilin University of Electrical Technology, Guilin 541004, China*
[d]*Center for Energy Harvesting Materials and System (CEHMS), Virginia Tech, Blacksburg, Virginia 24061, USA*

†Electronic supplementary information (ESI) available. See DOI: 10.1039/c7nr04501h

in the perovskite due to limited solubility of CsX compared with MAX, leading to mediocre solar cell efficiency.[34]

Vacuum evaporation has been demonstrated as an efficient method to fabricate uniform and pin-hole-free perovskite films with complete surface coverage.[35–37] Herein, we report our success in fabricating Cs-substituted $MA_{1-x}Cs_xPbI_3$ perovskite films using a vacuum co-evaporation deposition method. The resultant film is free of pin-holes, and is uniform with complete surface coverage. It is found that the band gap of the perovskite film can be fine-tuned within 1.605–1.651 eV by adjusting the Cs content. Detailed analyses show that the perovskite film has reduced trap-state density and longer carrier lifetime. Compared with the pristine perovskite without Cs, the PCE of the PSCs is increased from 15.84% to as high as 20.13% after the Cs substitution, which stands among the highest efficiency for planar PSCs. More importantly, the Cs-substituted PSCs using the vacuum co-evaporation method exhibit extraordinary stability compared with the pristine perovskite devices.

Results and discussion

Vacuum co-evaporation method

Scheme 1 illustrates the preparation process for Cs-substituted perovskite films *via* the vacuum co-evaporation deposition method. First, the $PbCl_2$ and CsCl were simultaneously evaporated on fluorine-doped tin oxide (FTO)/TiO_2 substrate at different evaporation rates in a vacuum chamber. Subsequently, a layer of MAI powder was placed on the film of $PbCl_2$–CsCl mixture. Upon heating to 150 °C for 20 minutes, $PbCl_2$ and CsCl were converted into the Cs-substituted perovskite. The color of the sample was changed from transparent to dark after annealing, suggesting the formation of $MA_{1-x}Cs_xPbI_3$ perovskite. The experimental details are given in the experimental section.

Properties of Cs-substituted perovskites

By controlling the individual rate of evaporation, the Cs-to-Pb ratio in the deposited film can be regulated. The composition and elemental distribution in the perovskite coating were measured by X-ray photoelectron spectroscopy (XPS), as shown in Fig. S1.† It is apparent that the Cs 3d characteristic peak appears at around 730 eV,[38] demonstrating that the Cs cations are effectively incorporated into the perovskite film. High-resolution Cs 3d and Pb 4f spectra are shown in Fig. S2,† with four peaks identified at 738.5, 724.6, 143.0 and 138.1 eV, corresponding to Cs 3d3/2, Cs 3d5/2, Pb 4f5/2 and Pb 4f7/2, respectively.[38,39] Fig. 1a presents Cs 3d peak intensity as a function of Cs content. The Cs-to-Pb ratio is estimated by the peak area weighted by atomic sensitivity factors for Cs 3d and Pb 4f. The calculated details are provided in ESI.† The ratios of Cs to Pb are 0, 0.11, 0.17, 0.23 and 0.34, corresponding to the CsCl evaporation rates of 0, 0.3, 0.45, 0.6 and 0.9 Å s^{-1}, respectively.

To gain insight into the Cs substitution on the crystallization of the $MAPbI_3$ perovskite, a series of perovskite films with different Cs contents was characterized by X-ray diffraction (XRD). Fig. 1b shows the XRD patterns for $MAPbI_3$ perovskite films with Cs contents of 0, 0.11, 0.17, 0.23 and 0.37. All typical perovskite peaks including (110), (112), (111), (211), (202), (220), (310), (224), (330) and (314) diffractions are clearly identified, indicating that the Cs substitution does not affect the crystallization. For clarity, Fig. 1c shows a zoomed-in version of the (110) diffraction peak for the $MA_{1-x}Cs_xPbI_3$ sample. The 2θ value monotonically shifts from 14.14° to 14.36° with the Cs content increasing from 0 to 0.34 due to the smaller Cs^+ radius (1.81 Å) compared to that of MA^+ (2.70 Å), which is in good agreement with literature,[22,40] demonstrating that the Cs cations are effectively integrated into the $MAPbI_3$ perovskite lattice. The Cs cation doping can improve the stability of the $MAPbI_3$ perovskite,[40,41] as will be discussed later.

The impact of the Cs substitution on the optical properties for the $MAPbI_3$ perovskite was studied using UV–Vis–NIR absorption measurement. Fig. 1d shows the absorption spectra of $MA_{1-x}Cs_xPbI_3$ perovskite with different Cs concentrations. It is found that as the Cs content is increased, its absorption peak shifts to a shorter wavelength and the band gap is enlarged, as shown in Fig. S3a.† A larger band gap is beneficial for attaining a higher V_{oc}, even though the J_{sc} may be moderated.[40] Fig. S3b† shows that the band gap increases linearly with Cs content, indicating that the band gap of $MA_{1-x}Cs_xPbI_3$ can be fine-tuned *via* Cs substitution.

To understand the charge recombination and transfer kinetics in the Cs-substituted perovskite films, steady-state photoluminescence (PL) and time-resolved PL (TRPL) measurements were carried out. As shown in Fig. 1e, the PL intensity of glass/$MA_{1-x}Cs_xPbI_3$ samples is sharply enhanced with the increase in the Cs content. However, when the Cs content is increased to 0.34, the PL intensity slightly decreases. Moreover, possibly due to the excess Cs, a large mismatch between Cs and MA is created, thus initiating phase separation.[42,43] It is found that the PL intensity enhancement is related to reduced trap-state density in the Cs-substituted perovskite films.[44] The normalized PL peaks (Fig. S4†) display blue-shift from 765 to 759 nm,

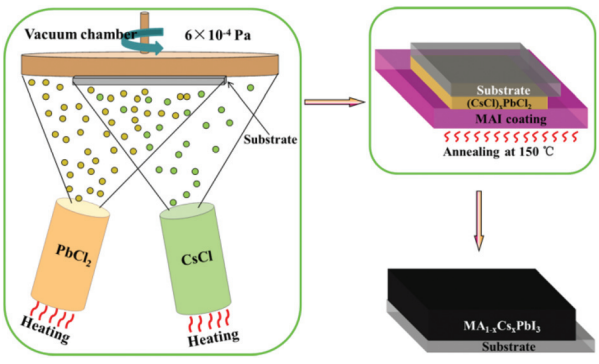

Scheme 1 Illustration of the vacuum co-evaporation method to deposit the Cs-substituted $MA_{1-x}Cs_xPbI_3$ perovskite thin film.

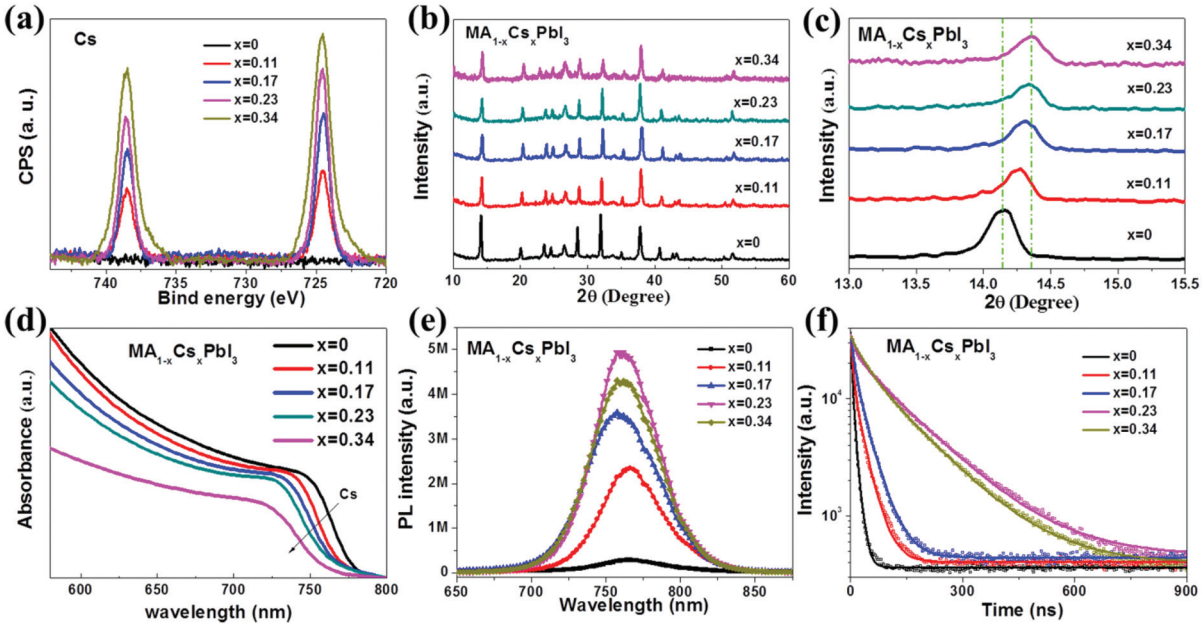

Fig. 1 (a) Cs 3d peak intensity as a function of Cs content. (b) XRD patterns of the $MA_{1-x}Cs_xPbI_3$ films. (c) XRD zoomed in on (110) diffraction peaks of perovskite based on various Cs contents. (d) UV–Vis absorption spectra of $MA_{1-x}Cs_xPbI_3$ films. (e) PL and (f) TRPL spectra of perovskite with different Cs contents deposited on glass substrates.

which is consistent with the trend shown in the UV–Vis–NIR absorption spectra.

TRPL characterization is recognized as an effective tool to monitor trap-state density in the perovskite films. Fig. 1f shows PL decay time (τ_i) and amplitudes (A_i) of the glass/$MA_{1-x}Cs_xPbI_3$ samples fitted by a bi-exponential decay function, with key parameters listed in Table S1.† It appears that the PL decay time of the pristine $MAPbI_3$ is τ_1 = 11.96 ns and τ_2 = 4.67 ns, with the corresponding amplitudes of 20.24% and 69.76%, respectively. When the Cs content is increased to 0.34, both τ_1 and τ_2 are increased to as much as 135.18 and 15.06 ns, with the corresponding amplitudes changed to 66.76% and 33.24%. The average recombination lifetime (τ_{ave}) can be estimated using eqn (1):[45]

$$\tau_{ave} = \frac{\sum A_i \tau_i^2}{\sum A_i \tau_i} \quad (1)$$

It turns out that while the average lifetime of the pristine $MAPbI_3$ perovskite is only 2.83 ns, it increases to 23.13, 31.73, 115.35 and 128.85 ns when the content of Cs substituted is gradually increased to 0.11, 0.17, 0.23 and 0.34, respectively. The long recombination lifetime is ascribed to the reduced trap-state density in the Cs-substituted perovskite film.[46] In addition, devices with the structure of FTO/perovskite/Au were fabricated, and the trap-state density was calculated by measuring the current–voltage (I–V) plot in the dark, as shown in Fig. S5.† The device based on x = 0.23 for the $MA_{1-x}Cs_xPbI_3$ perovskite film was chosen for comparison, and the calculation results demonstrate that the trap-state density in the perovskite film decreases from 1.16×10^{16} to 3.15×10^{15} cm^{-3} after the Cs substitution, which is in agreement with the previous observation and deduction that the Cs-substitution is conducive to lowering trap-state density. The reduced trap-state density is certainly desirable for improving the solar cell performance. More calculation details are given in ESI.†

Performance of PSCs based on $MA_{1-x}Cs_xPbI_3$ absorber

Given the above advantages achieved from the Cs-substitution of the $MAPbI_3$ perovskite, including reduced trap-state density, relaxed lattice strain, longer carrier lifetime and tunable band gap, devices based on the $MA_{1-x}Cs_xPbI_3$ perovskite film were fabricated. Fig. 2a illustrates the cross-sectional scanning elec-

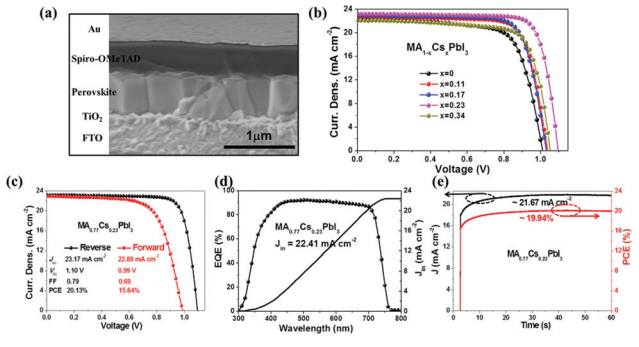

Fig. 2 (a) Representative cross-sectional SEM view of a complete device. (b) J–V characteristics of champion PSCs with different Cs contents. (c) J–V curves including reverse and forward scan directions of the champion PSC with $MA_{0.77}Cs_{0.23}PbI_3$ absorber. (d) EQE and the integrated product of the EQE curve with the AM 1.5G photon flux of $MA_{0.77}Cs_{0.23}PbI_3$ champion devices. (e) Photocurrent density and PCE measured as a function of time biased at 0.92 V for the $MA_{0.77}Cs_{0.23}PbI_3$ device.

tron microscopy (SEM) analysis of a complete device, wherein the compact TiO_2 film is used as the electron-transport layer, 2,2′,7,7′-tetrakis(*N*,*N*-di-*p*-methoxyphenylamine)-9,9′-spirobifluorene (spiro-OMeTAD) as the hole-transport layer, FTO and gold coating as the bottom and the top electrodes, respectively, and the $MAPbI_3$ perovskite with different Cs contents, fabricated by the vacuum co-evaporation deposition method, as the absorber. All fabrication details are shown in the Experimental section. The morphology of $MA_{1-x}Cs_xPbI_3$ films is characterized by top-view SEM image, as shown in Fig. S6.† It is clear that uniform, pin-hole-free perovskite films with good surface coverage are formed on TiO_2 substrates regardless of Cs contents. Furthermore, the energy-dispersive X-ray spectrometer (EDX) analysis (Fig. S7†) confirms that the Cs is homogeneously distributed throughout the perovskite films.

Fig. 2b shows the current density–voltage (*J*–*V*) curves of PSCs based on various Cs contents under AM 1.5G illumination at 100 mW cm^{-2}, and the key parameters including J_{sc}, V_{oc}, fill factor (FF), PCE, series resistance (R_s) and shunt resistance (R_{sh}) of each device are summarized in Table 1. It is clear that the PSC performance is significantly affected by the Cs content. The device parameters related to different Cs contents are shown in Fig. S8.† While the control device based on pristine $MAPbI_3$ gives a PCE = 15.84%, the PCE is improved to as high as 20.13% when the Cs content is increased to x = 0.23. In fact, all key *J*–*V* parameters including V_{oc}, FF and J_{sc} are systematically improved due to the smallest R_s and largest R_{sh}. Compared with that of the control device, the drastically increased V_{oc} is attributed to the widened band gap after the Cs substitution (Fig. S3†).[40] While the band gap of perovskite broadens with the increasing Cs content, the J_{sc} value is suddenly enhanced. When the Cs content is increased to x = 0.23, the J_{sc} and FF values increase to 23.17 mA cm^{-2} and 0.79, respectively. The FF and J_{sc} values are increased due to the reduced trap-state density (Fig. S5,† from 1.16×10^{16} to 3.15×10^{15} cm^{-3} compared with pure perovskite).[19,46] Overall, the PCE increases with the Cs content until, when the Cs content is increased to x = 0.34, the PCE decreases to 17.13% due to the aforementioned phase separation (Fig. S8†).[43,44] The Cs content x = 0.23 was found to be the optimum Cs substitution value. To demonstrate that the phenomenon is reproducible, more devices have been fabricated. Their statistics distributions are shown in Fig. S9,† and the key *J*–*V* parameters are listed in Tables S2 and S3.† Compared with that in the control devices, all *J*–*V* parameters using the $MA_{0.77}Cs_{0.23}PbI_3$ absorber give a more narrow distribution, demonstrating that the Cs-substitution is indeed reproducible.

Table 1 Key *J*–*V* parameters of the $MA_{1-x}Cs_xPbI_3$ devices

Cs content	J_{sc} (mA cm^{-2})	V_{oc} (V)	FF	PCE (%)	R_s (Ω)	R_{sh} (kΩ)
0	22.40	1.01	0.70	15.84	34.53	5.07
0.11	22.69	1.03	0.76	17.76	29.12	16.64
0.17	22.92	1.04	0.76	18.12	27.36	18.44
0.23	23.17	1.10	0.79	20.13	10.68	26.64
0.34	22.04	1.05	0.74	17.13	28.30	7.13

Fig. 2c shows the *J*–*V* curves of the champion PSC based on the $MA_{0.77}Cs_{0.23}PbI_3$ measured at reverse and forward scan directions. The device displays a PCE of 20.13% with a J_{sc} value of 23.17 mA cm^{-2}, a V_{oc} value of 1.10 V and an FF value of 0.79 under reverse scan direction, and 15.64% with a lower V_{oc} value of 0.99 V and an FF value of 0.69 under forward scan direction, discounted by ~22%. The awful hysteresis is attributed to ion migration, the unbalanced carrier transport or ferroelectric effect within the perovskite absorber.[47–49] Fig. 2d shows the external quantum efficiency (EQE) and the calculated J_{sc} values by integrating the EQE curves, which is 22.41 mA cm^{-2}, very close to the *J*–*V* measurements. In order to confirm the *J*–*V* measurement, the typical stabilized power output of the photocurrent density for the champion $MA_{0.77}Cs_{0.23}PbI_3$ solar cell was measured as a function of time when the device was biased at V_{mp} = 0.92 V (voltage at the maximum power point in the *J*–*V* plot), as shown in Fig. 2e. The photocurrent density and PCE stabilize at 21.67 mA cm^{-2} and 19.94%, respectively, extremely close to what is obtained from the *J*–*V* measurement. The maximum photocurrent density takes over 30 s to reach a steady value, caused by the hysteresis.[50]

Dark *J*–*V* and EIS analysis

The dark *J*–*V* analysis is often used to reveal the intrinsic characteristics of the solar cells. We measured the dark *J*–*V* of the champion devices using pristine $MAPbI_3$ and $MA_{0.77}Cs_{0.23}PbI_3$ absorbers, as shown in Fig. 3a. The dark *J*–*V* plot can be divided into three regions.[51] Region A often reflects the leakage current of the PSCs. It is clear that the leakage current of the $MA_{0.77}Cs_{0.23}PbI_3$ device is one order of magnitude lower than that of the pristine $MAPbI_3$ cell in the reverse direction, leading to higher J_{sc} and FF.[52] Region B depends on exponential diode comportment, while region C reveals that the R_s value of the $MA_{0.77}Cs_{0.23}PbI_3$ cell is larger than that of the control device, which is in good agreement with the irradiation *J*–*V* results. The V_{oc} value can be estimated using the following eqn (2):[53]

$$V_{oc} = \frac{kT}{q} \ln\left(\frac{J_t}{J_0} + 1\right) \quad (2)$$

where k is the Boltzmann constant, T the absolute temperature, q the elementary charge, J_t the theory of current density and J_0 the reverse saturation current density. It is clear that a smaller J_0 value would produce a larger V_{oc} value. J_0 can be obtained by fitting the dark *J*–*V* in region B, which is 2.61×10^{-5} for $MAPbI_3$ and 5.83×10^{-6} mA cm^{-2} for $MA_{0.77}Cs_{0.23}PbI_3$, further demonstrating that the devices based on $MA_{0.77}Cs_{0.23}PbI_3$ should have higher V_{oc} values.

The recombination resistance and transport resistance in the pristine $MAPbI_3$ and $MA_{0.77}Cs_{0.23}PbI_3$ solar cells were analyzed by electrical impedance spectroscopy (EIS). Fig. 3b shows the Nyquist plots in the dark condition with an applied voltage

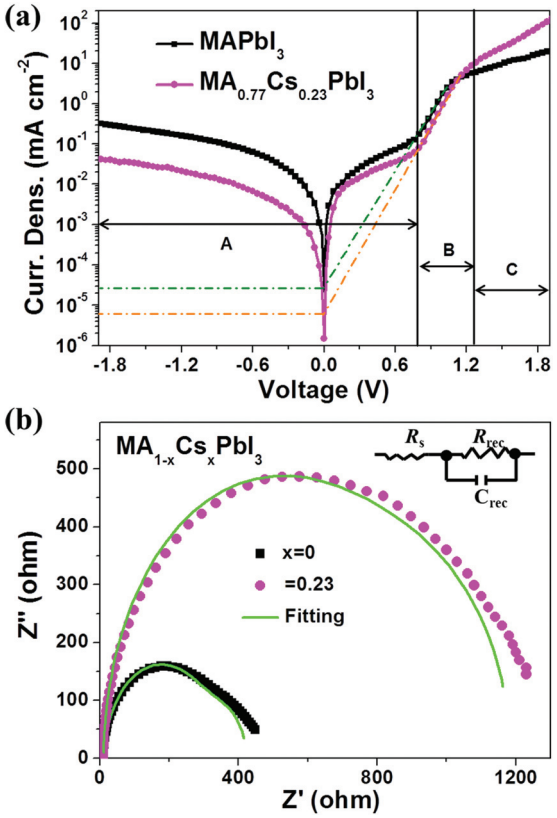

Fig. 3 (a) Dark J–V curves of champion devices using $MAPbI_3$ and $MA_{0.77}Cs_{0.23}PbI_3$. (b) EIS of PSCs with $MAPbI_3$ and $MA_{0.77}Cs_{0.23}PbI_3$; the inset gives the equivalent circuit for fitting the Nyquist plots.

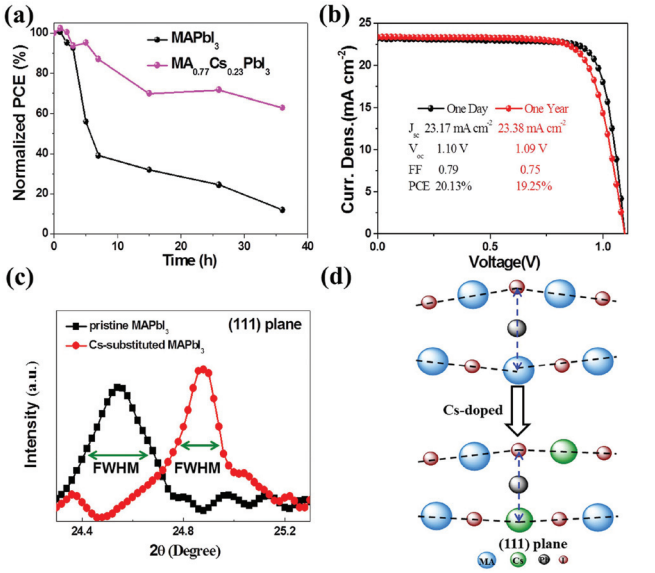

Fig. 4 (a) PCE stability of PSCs without encapsulation exposed to AM 1.5G irradiation in ambient air. (b) J–V characteristics of champion PSCs without encapsulation after storing in dark under ambient condition for over one year. (c) A close-up XRD characteristic centered at the (111) diffraction peak. (d) Schematic of strain relaxation after Cs substitution.

of V_{oc}, and the top-right inset gives the equivalent circuit composed of the R_s and the recombination resistance (R_{rec}). The R_{rec} is assigned to the high-frequency region in EIS.[54] The fitted parameters by the equivalent circuit are listed in Table S4.† The R_s values of the pristine $MAPbI_3$ and $MA_{0.77}Cs_{0.23}PbI_3$ solar cells are 36.27 and 11.75 Ω, respectively, which are very close to the results calculated from the J–V curves (Table 1). The smaller R_s would facilitate the carrier transport, leading to larger J_{sc}.[5] Interestingly, compared with the control device, the R_{rec} value of the $MA_{0.77}Cs_{0.23}PbI_3$ solar cell significantly increases to 1025 from 354 Ω, effectively suppressing the charge recombination, and therefore, facilitating improved device performance.[55]

Stability of PSCs

Compared with the solution-processed methods, the vacuum co-evaporation deposition method provides high-quality, large-area uniform perovskite materials. It is expected that it is more compact and, therefore, more resistant to moisture, resulting in better device stability.[35] We measured the sustained irradiation stability of the bare device without encapsulation. As shown in Fig. 4a, the PCE of the Cs-substituted device shows a higher stability than the pristine $MAPbI_3$ cell. The PCE remained at ~63% of its initial value for the $MA_{0.77}Cs_{0.23}PbI_3$ device after being irradiated for 36 h, whereas the PCE of the pristine $MAPbI_3$ cell dropped by ~88% compared with its initial efficiency under the same illumination conditions. A minor increase in the performance at the primary stage may be ascribed to the oxidation of spiro-OMeTAD.[56] It is very exciting that the bare device without any encapsulation exhibits extremely high stability though stored in dark in ambient air for over one year. As shown in Fig. 4b, after storing the Cs-substituted PSC in dark for one year, the PCE remains at 19.25% with J_{sc} = 23.38 mA cm^{-2}, V_{oc} = 1.09 V and FF = 0.75, degrading only 4.37% of the initial efficiency.

The excellent stability of the Cs-substituted PSCs originated from the high purity of the crystalline phase (Fig. 1b) and the lower trap-state density (Fig. S5†) of perovskite films, as well as reduced lattice constant and relaxed strain caused by Cs substitution.[35,40] It is well known that the lattice structure plays an important role in the stability of perovskite materials.[22] Fig. 4c shows a close-up XRD characteristic centered at the (111) peak. It is clear that the peak is shifted toward a larger angle after Cs substitution, indicating that the interplanar spacing is reduced according to Bragg's law ($n\lambda = 2d_{hkl}\sin\theta$). As a result, the lattice constant is reduced to 6.199 from 6.285 Å as calculated in the following equation:

$$a = \frac{d_{hkl}}{\sqrt{h^2 + k^2 + l^2}} \quad (3)$$

where a is the lattice constant, d_{hkl} is the interplanar spacing of the (hkl) plane, and h, k and l are the Miller indices. Moreover, Fig. 4c shows that the (111) peak width, as defined by the full width at half maximum (FWHM), of the Cs-substituted sample is significantly narrowed compared with that of

the pristine $MAPbI_3$, demonstrating smaller strain in the (111) plane because of the interplanar distance deviation.[41] The plane strain in the Cs-substituted perovskite framework is relaxed, as shown in Fig. 4d. We therefore infer that the smaller lattice and moderate plane strain facilitate the improvement of stability of perovskite.[40,41]

Conclusions

In this study, we first used the vacuum co-evaporation deposition method to fabricate high-quality pin-hole-free Cs-substituted perovskite films with uniform crystal grains. The Cs-substitution brings several advantages including reduced trap-state density, tuned band gap, and longer carrier lifetime. The PCE of the device based on $MA_{0.77}Cs_{0.23}PbI_3$ is as high as 20.13%, increased by ~27% compared with the pristine $MAPbI_3$-based solar cell, which is among the highest reported for planar PSCs. Moreover, the Cs-substituted PSCs without encapsulation exhibit better stability regardless of dark and continued irradiation. We attribute it to the reduced lattice parameter and relaxed strain in perovskite caused by Cs substitution, demonstrating that the vacuum co-evaporation deposition method is an effective technique to manufacture PSCs with good stability and high performance.

Experimental

Substrate preparation

The FTO glass was cleaned with acetone, isopropyl alcohol, ethyl alcohol and deionized water successively in a sonication bath for 30 min and then dried by flowing nitrogen gas, followed by treatment in an ultraviolet-ozone chamber (Ultraviolet Ozone Cleaned, Jelight Company USA) for 15 min. The compact TiO_2 layers were fabricated according to a previous report.[57] Yellow polyimide tapes were kept at the front side for the purpose of contact, to ensure that there is no deposition of TiO_2 at the edges. The $TiCl_4$ (4.49 mL) was slowly dropped in the ice, and then the solution was diluted to a concentration of 0.2 mol L^{-1}. The FTO substrates with the tapes were immersed into the $TiCl_4$ solution and kept in an oven at 70 °C for 45 min. The FTO/TiO_2 substrates were washed with water and dried by flowing nitrogen gas. The thickness of the TiO_2 film was determined to be ~45 nm by the Bruker 150 surface profiler.

Device fabrication

The perovskite films were deposited onto the TiO_2 substrates using the vacuum co-evaporation deposition method. First, the $PbCl_2$ without and with Cs-substituted films was deposited on 25 × 25 mm^2 substrates by a thermal evaporation system (Scheme 1). First, the $PbCl_2$ films of suitable thickness were fabricated at a rate of ~3 Å s^{-1} by evaporation at ~350 °C. During $PbCl_2$ deposition, the CsCl was simultaneously evaporated at ~430–445 °C with evaporation rates of 0.3, 0.45, 0.6 and 0.9 Å s^{-1} to obtain the $PbCl_2$ films with different Cs contents. When the ceramic crucible boats for $PbCl_2$ and CsCl were cooled to room temperature after about 1 hour, the samples were transferred into the nitrogen-filled glovebox. The MAI powder was placed into a 70 mm × 70 mm aluminum reactor to form a ~0.5 mm thick uniform and compact thin film. Then, the samples were placed on a layer of MAI powder, and heated to 150 °C for 20 min to ensure transformation of $PbCl_2$ and CsCl into perovskite. Finally, the perovskite samples were transferred into a petri dish, cooled for 30 min, washed with 50 mL isopropanol, and dried by flowing nitrogen gas. The thickness of the perovskite film was determined to be ~532 nm by cross-sectional SEM (Fig. 2a). The 90 mg mL^{-1} spiro-OMeTAD chlorobenzene solution, with 36 μL *t*-BP and 22 μL of a solution of 520 mg mL^{-1} Li-TFSI in acetonitrile added, was spin-coated onto the perovskite films at 5000 rpm for 30 s. The thickness of the spiro-OMeTAD film was determined to be ~340 nm by cross-sectional SEM analysis (Fig. 2a). Finally, an 80 nm Au electrode was deposited using a thermal evaporator.

Characterization

The *J*–*V* curves of the PSCs were characterized by Keithley 2400 Source under ambient conditions. The illumination intensity was calibrated to 100 mW cm^{-2} by a NREL-traceable KG5-filtered silicon reference cell. The device area of 9 mm^2 was defined by a metal mask. The devices were scanned from V_{oc} to J_{sc} (reverse) and from J_{sc} to V_{oc} (forward) at a scan rate of 0.1 V s^{-1}. The EQE was carried out using the QTest Station 2000ADI system (Crowntech. Inc., USA). A 150 W halogen tungsten lamp was used as the light source, and the monochromatic light intensity for the EQE was calibrated using a reference silicon photodiode. The TRPL spectra were recorded on the Edinburgh Instruments FLS920 fluorescence spectrometer using the time-correlated single-photon counting method. A picosecond pulsed diode laser at 406.8 nm with a pulse width of 64.2 ps was used as the excitation source. SEM images were obtained using a field emission scanning electron microscope (SU8020) under an accelerating voltage of 5 kV. The XRD patterns were tested using the SmartLab X-ray diffraction system. XPS spectra were measured on the AXISULTRA X-ray photoelectron spectrometer using Al Kα as the excitation X-ray source under a pressure of 5 × 10^{-7} Pa. The UV–Vis absorption spectra were acquired by the Hitachi U-3900 spectrophotometer.

Conflicts of interest

The authors declare no competing financial interests.

Acknowledgements

The authors acknowledge all the support from the National Natural Science Foundation of China (61604090 and

61674098), the National Key Research Program of China (2016YFA0202403), the National University Research Fund (GK261001009), the Innovative Research Team (IRT_14R33) and the Chinese National 1000-talent-plan program.

Notes and references

1 Y. Li, L. Meng, Y. M. Yang, G. Xu, Z. Hong, Q. Chen, J. You, G. Li, Y. Yang and Y. Li, *Nat. Commun.*, 2016, **7**, 10214.
2 S. D. Stranks, G. E. Eperon, G. Grancini, C. Menelaou, M. J. P. Alcocer, T. Leijtens, L. M. Herz, A. Petrozza and H. J. Snaith, *Science*, 2013, **342**, 341.
3 Q. Dong, Y. Yuan, Y. Shao, Y. Fang, Q. Wang and J. Huang, *Energy Environ. Sci.*, 2015, **8**, 2464.
4 J. S. Manser and P. V. Kamat, *Nat. Photonics*, 2014, **8**, 737.
5 D. Yang, R. Yang, J. Zhang, Z. Yang, S. Liu and C. Li, *Energy Environ. Sci.*, 2015, **8**, 3208.
6 A. Kojima, K. Teshima, Y. Shirai and T. Miyasaka, *J. Am. Chem. Soc.*, 2009, **131**, 6050.
7 D. Son, J. Lee, Y. J. Choi, I. Jang, S. Lee, P. J. Yoo, H. Shin, N. Ahn, M. Choi, D. Kim and N. Park, *Nat. Energy*, 2016, **1**, 16081.
8 J. Correa-Baena, M. Anaya, G. Lozano, W. Tress, K. Domanski, M. Saliba, T. Matsui, T. J. Jacobsson, M. E. Calvo, A. Abate, M. Grätzel and H. Míguez, *Adv. Mater.*, 2016, **28**, 5031.
9 X. Li, D. Bi, C. Yi, J.-D. Décoppet, J. Luo, S. M. Zakeeruddin, A. Hagfeldt and M. Grätzel, *Science*, 2016, **353**, 6294.
10 NREL Efficiency Chart, http://www.nrel.gov/pv/assets/images/efficiency_chart.jpg.
11 O. Malinkiewicz, A. Yella, Y. H. Lee, G. M. Espallargas, M. Graetzel, M. K. Nazeeruddin and H. J. Bolink, *Nat. Photonics*, 2014, **8**, 128.
12 H. Zhou, Q. Chen, G. Li, S. Luo, T.-b. Song, H.-S. Duan, Z. Hong, J. You, Y. Liu and Y. Yang, *Science*, 2014, **345**, 542.
13 D. Liu and T. L. Kelly, *Nat. Photonics*, 2014, **8**, 133.
14 N. J. Jeon, J. H. Noh, Y. C. Kim, W. S. Yang, S. Ryu and S. Seok, *Nat. Mater.*, 2014, **13**, 897.
15 D. Bi, W. Tress, M. I. Dar, P. Gao, J. Luo, C. Renevier, K. Schenk, A. Abate, F. Giordano, J.-P. C. Baena, J.-D. Decoppet, S. M. Zakeeruddin, M. K. Nazeeruddin, M. Grätzel and A. Hagfeldt, *Sci. Adv.*, 2016, **2**, e1501170.
16 N. J. Jeon, J. H. Noh, W. S. Yang, Y. C. Kim, S. Ryu, J. Seo and S. Seok, *Nature*, 2015, **517**, 476.
17 Y. Liu, Z. Yang, D. Cui, X. Ren, J. Sun, X. Liu, J. Zhang, Q. Wei, H. Fan, F. Yu, X. Zhang, C. Zhao and S. Liu, *Adv. Mater.*, 2015, **27**, 5176.
18 G. Xing, N. Mathews, S. Sun, S. S. Lim, Y. M. Lam, M. Grätzel, S. Mhaisalkar and T. C. Sum, *Science*, 2013, **342**, 344.
19 D. Yang, R. Yang, X. Ren, X. Zhu, Z. Yang, C. Li and S. Liu, *Adv. Mater.*, 2016, **28**, 5206.
20 Q. Guo, C. L. W. Qiao, S. Ma, F. Wang, B. Zhang, L. Hu, S. Dai and Z. Tan, *Energy Environ. Sci.*, 2016, **9**, 1486.
21 Q. Wei, D. Yang, Z. Yang, X. Ren, Y. Liu, J. Feng, X. Zhu and S. Liu, *RSC Adv.*, 2016, **6**, 56807.
22 D. P. McMeekin, G. Sadoughi, W. Rehman, G. E. Eperon, M. Saliba, M. T. Hörantner, A. Haghighirad, N. Sakai, L. Korte, B. Rech, M. B. Johnston, L. M. Herz and H. J. Snaith, *Science*, 2016, **351**, 151.
23 Y. Liu, Y. Zhang, Z. Yang, D. Yang, X. Ren, L. Pang and S. Liu, *Adv. Mater.*, 2016, **28**, 9204–9209.
24 Y. Li, W. Sun, W. Yan, S. Ye, H. Rao, H. Peng, Z. Zhao, Z. Bian, Z. Liu, H. Zhou and C. Huang, *Adv. Energy Mater.*, 2016, **6**, 1601353.
25 T. Krishnamoorthy, H. Ding, C. Yan, W. L. Leong, T. Baikie, Z. Zhang, M. Sherburne, S. Li, M. Asta, N. Mathews and S. G. Mhaisalkar, *J. Mater. Chem. A*, 2015, **3**, 23829.
26 M. B. Johansson, H. Zhu and E. M. J. Johansson, *J. Phys. Chem. Lett.*, 2016, **7**, 3467.
27 N. Pellet, P. Gao, G. Gregori, T.-Y. Yang, M. K. Nazeeruddin, J. Maier and M. Grätzel, *Angew. Chem., Int. Ed.*, 2014, **53**, 3151.
28 J.-W. Lee, D.-H. Kim, H.-S. Kim, S.-W. Seo, S. M. Cho and N.-G. Park, *Adv. Energy Mater.*, 2015, **5**, 1501310.
29 H. Choi, J. Jeong, H.-B. Kim, S. Kim, B. Walker, G.-H. Kim and J. Y. Kim, *Nano Energy*, 2014, **7**, 80.
30 W. Ke, C. Xiao, C. Wang, B. Saparov, H.-S. Duan, D. Zhao, Z. Xiao, P. Schulz, S. P. Harvey, W. Liao, W. Meng, Y. Yu, A. J. Cimaroli, C.-S. Jiang, K. Zhu, M. Al-Jassim, G. Fang and D. B. Mitzi, *Adv. Mater.*, 2016, **28**, 5214.
31 S.-S. Li, C.-H. Chang, Y.-C. Wang, C.-W. Lin, D.-Y. Wang, J.-C. Lin, C.-C. Chen, H.-S. Sheu, H.-C. Chia, W.-R. Wu, U. Jeng, C.-T. Liang, R. Sankar, F.-C. g. Chou and C.-W. Chen, *Energy Environ. Sci.*, 2016, **9**, 1282.
32 Y. Xu, L. Zhu, J. Shi, S. Lv, X. Xu, J. Xiao, J. Dong, H. Wu, Y. Luo, D. Li and Q. Meng, *ACS Appl. Mater. Interfaces*, 2015, **7**, 2242.
33 W. Zhang, M. Saliba, D. T. Moore, S. K. Pathak, M. T. Hörantner, T. Stergiopoulos, S. D. Stranks, G. E. Eperon, J. A. Alexander-Webber, A. Abate, A. Sadhanala, S. Yao, Y. Chen, R. H. Friend, L. A. Estroff, U. Wiesner and H. J. Snaith, *Nat. Commun.*, 2015, **6**, 6142.
34 G. Niu, H. Yu, J. Li, D. Wang and L. Wang, *Nano Energy*, 2016, **27**, 87.
35 D. Yang, Z. Yang, W. Qin, Y. Zhang, S. Liu and C. Li, *J. Mater. Chem. A*, 2015, **3**, 9401.
36 M. Liu, M. B. Johnston and H. J. Snaith, *Nature*, 2013, **501**, 395.
37 C. Momblona, L. Gil-Escrig, E. Bandiello, *et al.*, *Energy Environ. Sci.*, 2016, **11**, 3456.
38 R. D. Mathews, A. R. Slaughter, R. J. Key and M. S. Banna, *J. Chem. Phys.*, 1983, **78**, 62.
39 Y. Ogomi, A. Morita, S. Tsukamoto, T. Saitho, N. Fujikawa, Q. Shen, T. Toyoda, K. Yoshino, S. S. Pandey, T. Ma and S. Hayase, *J. Phys. Chem. Lett.*, 2014, **5**, 1004.
40 M. Saliba, T. Matsui, J.-Y. Seo, K. Domanski, J.-P. Correa-Baena, M. K. Nazeeruddin, S. M. Zakeeruddin, W. Tress, A. Abate, A. Hagfeldt and M. Grätzel, *Energy Environ. Sci.*, 2016, **9**, 1989.

41 K. H. Ahn, T. Lookman and A. R. Bishop, *Nature*, 2014, **428**, 401.
42 Z. Li, M. Yang, J.-S. Park, S.-H. Wei, J. J. Berry and K. Zhu, *Chem. Mater.*, 2016, **28**, 284.
43 C. Yi, J. Luo, S. Meloni, A. Boziki, N. Ashari-Astani, C. Grätzel, S. M. Zakeeruddin, U. Röthlisberger and M. Grätzel, *Energy Environ. Sci.*, 2016, **9**, 656.
44 Q. Liang, J. Liu, Z. Cheng, Y. Li, L. Chen, R. Zhang, J. Zhang and Y. Han, *J. Mater. Chem. A*, 2016, **4**, 223.
45 B. Wu, K. Fu, N. Yantara, G. Xing, S. Sun, T. C. Sum and N. Mathews, *Adv. Energy Mater.*, 2015, **5**, 1500829.
46 J. You, Z. Hong, Y. M. Yang, Q. Chen, M. Cai, T.-B. Song, C.-C. Chen, S. Lu, Y. Liu, H. Zhou and Y. Yang, *ACS Nano*, 2014, **8**, 1674.
47 J. H. Heo, D. H. Song, H. J. Han, S. Y. Kim, J. H. Kim, D. Kim, H. W. Shin, T. K. Ahn, C. Wolf, T.-W. Lee and S. H. Im, *Adv. Mater.*, 2015, **27**, 3424.
48 S. V. Reenen, M. Kemerink and H. J. Snaith, *J. Phys. Chem. Lett.*, 2015, **6**, 3808.
49 J. Wei, Y. Zhao, H. Li, G. Li, J. Pan, D. Xu, Q. Zhao and D. Yu, *J. Phys. Chem. Lett.*, 2014, **5**, 3937.
50 J. H. Heo, H. J. Han, D. Kim, T. K. Ahn and S. H. Im, *Energy Environ. Sci.*, 2015, **8**, 1602.
51 J. Sheng, D. Wang, S. Wu, X. Yang, L. Ding, J. Zhu, J. Fang, P. Gao and J. Ye, *RSC Adv.*, 2016, **6**, 16010.
52 D. Yang, P. Fu, F. Zhang, N. Wang, J. Zhang and C. Li, *J. Mater. Chem. A*, 2014, **2**, 17281.
53 K. Vandewal, K. Tvingstedt, A. Gadisa, O. Inganäs and J. V. Manca, *Phys. Rev. B: Condens. Matter*, 2010, **81**, 12524.
54 P. Tiwana, P. Docampo, M. B. Johnston, H. J. Snaith and L. M. Herz, *ACS Nano*, 2011, **5**, 5158.
55 D. Yang, X. Zhou, R. Yang, Z. Yang, W. Yu, X. Wang, C. Li, S. Liu and R. P. H. Chang, *Energy Environ. Sci.*, 2016, **9**, 3071.
56 W. H. Nguyen, C. D. Bailie, E. L. Unger and M. D. McGehee, *J. Am. Chem. Soc.*, 2014, **136**, 10996.
57 A. Yella, L.-P. Heiniger, P. Gao, M. K. Nazeeruddin and M. Grätzel, *Nano Lett.*, 2014, **14**, 2591.